JOURNAL OF PROPULSION AND POWER
Vol. 24, No. 6, November–December 2008

Inert Particles for Axial-Combustion-Instability Suppression in a Solid Rocket Motor

David R. Greatrix*
Ryerson University, Toronto, Ontario M5B 2K3, Canada

DOI: 10.2514/1.34637

Various factors and trends related to the presence of inert particles in the central core flow as a means to suppress axial-combustion-instability symptom development are numerically predicted for a composite-propellant cylindrical-grain motor. Individual transient internal-ballistic-simulation runs show the evolution of the axial pressure wave and associated base pressure shift for a given inert particle size and loading percentage, as initiated by a given pressure disturbance. The pressure wave's limit magnitude at a later reference time in a given firing simulation run is collected for a series of runs at different particle sizes and loadings and is mapped onto an attenuation trend chart in a format potentially useful for motor designers evaluating their specific motor design and particle loading requirements (and, in turn, allowing for less experimental test firings, if the numerical results are relatively accurate). When the effect of acceleration (through structural vibration of the propellant surface) on the combustion process is included in the numerical calculations, one observes substantial differences in burning and internal flow behavior in the presence of axial-pressure-wave activity, as reflected in individual firing simulations and the corresponding particle attenuation map. The predicted base pressure shift is more pronounced at lower particle loadings: for example, in conjunction with the pressure-wave magnitude being larger, when the propellant's burning process is substantially sensitive to normal acceleration. Whether the propellant's burning rate is acceleration-sensitive or not, the inert particles' presence in the central core flow is demonstrated to be an effective means of suppression, correlating with past experimental successes in the usage of particles. Particle/burning-surface interactions, which may also act to suppress pressure-wave development by changing the propellant's inherent frequency-dependent combustion response, are not explicitly accounted for in this study, although one or two of the combustion-response model's pertinent coefficients could be altered to reflect this change, given sufficient information in this regard.

Nomenclature

A	=	local core cross-sectional area, m^2
a_ℓ	=	longitudinal (or lateral) acceleration, m/s^2
a_n	=	normal acceleration, m/s^2
C	=	de St. Robert's coefficient, $m/s \cdot Pa^n$
C_m	=	particle specific heat, $J/kg \cdot K$
C_p	=	gas specific heat, $J/kg \cdot K$
C_s	=	specific heat of the solid phase, $J/kg \cdot K$
d	=	local core hydraulic diameter, m
d_m	=	mean particle diameter, m
E	=	local total specific energy of gas in the core, J/kg
E_p	=	local total specific energy of the particle phase in the flow, J/kg
f	=	frequency, Hz
f	=	Darcy–Weisbach friction factor
G_a	=	accelerative mass flux, $kg/m^2 \cdot s$
h	=	convective heat transfer coefficient, $W/m^2 \cdot K$
K_b	=	burning-rate-limiting coefficient, s^{-1}
k	=	gas thermal conductivity, $W/m \cdot K$
k_s	=	thermal conductivity of the solid phase, $W/m \cdot K$
M_a	=	magnitude of attenuation
M_ℓ	=	limit magnitude resulting from cyclic input
m_p	=	mean mass of a particle, kg
n	=	exponent of de St. Robert's law
p	=	local gas static pressure, Pa
R	=	specific gas constant, $J/kg \cdot K$
r_b	=	instantaneous burning rate, m/s
$r_{b,o}$	=	reference burning rate, m/s
$r_{b,\mathrm{qs}}$	=	quasi-steady burning rate, m/s
r_b^*	=	unconstrained burning rate, m/s
r_o	=	base burning rate, m/s
T_f	=	flame temperature of the gas phase, K
T_i	=	initial temperature of the solid phase, K
T_s	=	burning-surface temperature, K
u	=	core axial gas velocity, m/s
u_p	=	core axial particle velocity, m/s
v_f	=	nominal flame-front velocity, m/s
x	=	distance from the head end, m
y	=	radial distance from burning surface, m
α_p	=	particle mass fraction of the overall core flow
α_s	=	thermal diffusivity of the solid phase, m^2/s
Δp_d	=	initial pulse disturbance step pressure, Pa
ΔH_s	=	net surface heat of the reaction, J/kg
Δt	=	time increment, s
Δx	=	spatial increment in the axial direction, m
Δy	=	spatial increment in the radial direction of the solid phase, m
Δy_{Fo}	=	Fourier limit spatial increment, m
δ_o	=	reference combustion-zone thickness, m
δ_r	=	resultant combustion-zone thickness, m
κ	=	vibration-based wall dilatation term $(1/A \cdot \partial A/\partial t)$, s^{-1}
ρ	=	gas density, kg/m^3
ρ_m	=	solid density of particle, kg/m^3
ρ_p	=	density of the particle phase in core flow, kg/m^3
ρ_s	=	solid density of propellant, kg/m^3
ϕ	=	acceleration orientation angle, rad
ϕ_d	=	long./lateral-acceleration-based displacement orientation angle, rad

Presented as Paper 5804 at the 43rd AIAA/ASME/SAE/ASEE Joint Propulsion Conference and Exhibit, Cincinnati, OH, 8–11 July 2007; received 18 September 2007; revision received 14 May 2008; accepted for publication 5 September 2008.

*Associate Professor, Department of Aerospace Engineering, 350 Victoria Street. Senior Member AIAA.

I. Introduction

OVER the last number of decades, a multitude of research efforts have been directed toward understanding the physical

mechanisms, or at least the surrounding factors, behind the appearance of symptoms typically associated with nonlinear axial combustion instability in solid-propellant rocket motors (SRMs). The principal symptoms are the presence within the motor chamber of stronger finite-amplitude traveling axial pressure waves that may be shock-fronted, commonly (although not always) accompanied by some degree of base chamber-pressure rise (dc shift). Note that low-magnitude pressure waves due to vortex-shedding from segmented/gapped components in the motor chamber are not included (here) in this more traditional category of nonlinear axial instability. Studies of nonlinear axial combustion instability have ranged from numerous experimental test-firing series [1] to linear/nonlinear acoustic-theory modeling [2–5]. Largely, the acoustic analysis produces frequency-based standing-wave solutions for a given chamber geometry, but without some useful quantitative information. On occasion, researchers have employed a numerical modeling approach to work toward a more comprehensive quantitative understanding of the physics involved. The numerical model produces a traveling-wave solution to a limit wave amplitude and a corresponding small or larger dc shift (typically, a time-based result evolving from an initial pulse disturbance introduced into the chamber flow [6,7]). Available computational power and associated result turnaround times commonly forced some simplifications in the given numerical model.

The motivation for the experimental, analytical, and numerical studies noted earlier was and is, of course, to bring a better understanding to bear in more precisely suppressing, if not eliminating, these axial-instability symptoms. For example, it has been long known that inert (nonreactive) or reactive particles in the internal core flow can help to suppress axial-combustion-instability symptoms [8–10]. As pointed out by Blomshield [11] in his wide-ranging review of a number of cases of different motors experiencing combustion instability over the years, it is not always clear as to the quantity of particle loading (and corresponding particle size) that is needed to adequately suppress the given symptoms, if that is the suppression technique being exploited. An additional potential complication pointed out by Waesche [10] is that it is not always clear that the effectiveness of particle or additive loading is due entirely to particle/drag effects within the central core flow or, in fact, is (in part or in whole) due to an altered combustion response of the propellant as a result of the presence of the particle/additive at the burning surface before entering the core-flow region. Waesche suggested that this effect may be more readily observed for reactive particles, rather than inert ones, considering the heat transfer effects in the solid phase [10]. Given this background on observations from past experiments, it would be advantageous to have a predictive numerical simulation model that, by incorporating at least some of the physical influences observed earlier, would help establish the particle loading/sizing requirement for a given SRM (in this case, for inert particles).

An effective numerical model combines the effects of the unsteady one- or two-phase flow, the transient-combustion process, and the structural dynamics of the surrounding propellant/casing structure. A case study reported by Blomshield [11], in which the changing of a heavyweight static-test-motor casing to a lightweight casing structure led to the appearance of combustion-instability symptoms, provides one motivation for inclusion of structural effects in the numerical model. Recent experimental observations by Dotson and Sako [12] on in-flight fluid–structure-interaction effects lend further weight in this regard. In the present investigation, an updated numerical model incorporating the preceding attributes is used in the prediction of the unsteady instability-related behavior in a cylindrical-grain motor and allows for an evaluation of the corresponding effectiveness of inert spherical particles at suppressing instability symptoms. It should be noted that particles and additives may not have, in practice, a spherical shape; for example, flakes of aluminum were used in an instability suppression study by Waesche [10].

II. Numerical Model

A simplified schematic diagram of the physical system of an SRM placed on a static-test stand is provided in Fig. 1. In this case, the cylindrical-grain motor is free to vibrate radially without any external constraint (i.e., only constrained as indicated by the thick steel static-test sleeve surrounding the aluminum lightweight motor casing), whereas axial motion is constrained to a large degree by the thrust-measuring load cell (represented here as a spring/damper) at the left-hand boundary. Under normal (nominal) quasi-equilibrium operating conditions, the internal gas flow (or gas–particle flow, if two-phase) moves smoothly from the burning propellant surface through and beyond the exhaust nozzle.

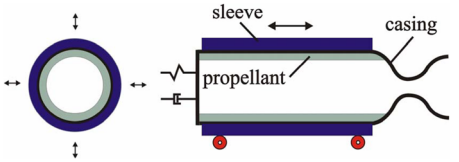

Fig. 1 Reference SRM model setup for static-test-stand firing.

A. Equations of Motion Governing Two-Phase Flow

The equations of motion describing the nonsteady core flow within the SRM must be solved in conjunction with the local pyrolysis rate r_b of the solid propellant and the surrounding structure's instantaneous geometric deformation. As pertains to the present study of a small motor with a larger length-to-diameter ratio, the quasi-one-dimensional hydrodynamic conservation equations for the axial gas flow are given next:

$$\frac{\partial \rho}{\partial t} + \frac{\partial(\rho u)}{\partial x} = -\frac{1}{A}\frac{\partial A}{\partial x}\rho u + (1-\alpha_p)\rho_s \frac{4r_b}{d} - \left(\frac{4r_b}{d} + \kappa\right)\rho \quad (1)$$

$$\frac{\partial(\rho u)}{\partial t} + \frac{\partial}{\partial x}(\rho u^2 + p) = -\frac{1}{A}\frac{\partial A}{\partial x}\rho u^2 - \left(\frac{4r_b}{d} + \kappa\right)\rho u - \rho a_\ell - \frac{\rho_p}{m_p}D \quad (2)$$

$$\frac{\partial(\rho E)}{\partial t} + \frac{\partial}{\partial x}(\rho u E + u p) = -\frac{1}{A}\frac{\partial A}{\partial x}(\rho u E + u p) - \left(\frac{4r_b}{d} + \kappa\right)\rho E + (1-\alpha_p)\rho_s \frac{4r_b}{d}\left(C_p T_f + \frac{v_f^2}{2}\right) - \rho u a_\ell - \frac{\rho_p}{m_p}(u_p D + Q) \quad (3)$$

where the total specific energy of the gas is defined for an ideal gas as $E = p/[(\gamma-1)\rho] + u^2/2$. The corresponding equations of motion for an inert (nonburning) particle phase within the axial flow may be found from

$$\frac{\partial \rho_p}{\partial t} + \frac{\partial(\rho_p u_p)}{\partial x} = -\frac{1}{A}\frac{\partial A}{\partial x}\rho_p u_p + \alpha_p \rho_s \frac{4r_b}{d} - \left(\frac{4r_b}{d} + \kappa\right)\rho_p \quad (4)$$

$$\frac{\partial(\rho_p u_p)}{\partial t} + \frac{\partial(\rho_p u_p^2)}{\partial x} = -\frac{1}{A}\frac{\partial A}{\partial x}\rho_p u_p^2 - \left(\frac{4r_b}{d} + \kappa\right)\rho_p u_p - \rho_p a_\ell + \frac{\rho_p}{m_p}D \quad (5)$$

$$\frac{\partial(\rho_p E_p)}{\partial t} + \frac{\partial(\rho_p u_p E_p)}{\partial x} = -\frac{1}{A}\frac{\partial A}{\partial x}(\rho_p u_p E_p) - \left(\frac{4r_b}{d} + \kappa\right)\rho_p E_p + \alpha_p \rho_s \frac{4r_b}{d}\left(C_m T_f + \frac{v_f^2}{2}\right) - \rho_p u_p a_\ell + \frac{\rho_p}{m_p}(u_p D + Q) \quad (6)$$

where the total specific energy of a local grouping of particles is given by $E_p = C_m T_p + u_p^2/2$, where T_p is the mean temperature of that group. As outlined in [13], the viscous interaction between the gas and particle phases is represented by the drag force D, and the

heat transfer from the core flow to the particles is defined by Q. In the case of drag between the gas and a representative spherical particle at a given axial location, one notes that

$$D = \frac{\pi d_m^2}{8} C_d \rho (u - u_p)|u - u_p| \tag{7}$$

where C_d is the drag coefficient for a sphere in a steady flow with low flow turbulence (determined as function of relative Reynolds number, relative flow Mach number, and temperature difference between the particle and the gas). In the case of heat transfer from the core flow to a representative particle at a given axial location, the following applies:

$$Q = \pi d_m k \cdot Nu \cdot (T - T_p) \tag{8}$$

where the Nusselt number Nu can be found as a function of the Prandtl and relative Reynolds numbers for a sphere of mean diameter d_m.

Longitudinal acceleration a_ℓ appears in the gas and particle momentum and energy equations as a body-force contribution within a fixed Eulerian reference (fixing of $x = 0$ to the motor head end with x positive and moving right on the structure, as per Fig. 1; acceleration of local surrounding structure rightward is designated as positive a_ℓ) and may vary both spatially along the length of the motor and with time. The effects of such factors as turbulence can be included through one or more additional equations that employ the information from the bulk-flow properties arising from the solution of the preceding one-dimensional equations of motion. The principal differential equations themselves can be solved via a higher-order, explicit, finite volume, random-choice-method approach: a Riemann-solution technique noted for low artificial dispersion with time of wave activity in tubes, etc., [13,14]. The equations of motion of the gas and particles will be solved over a given time step Δt (on the order of 1×10^{-7} s for the present study, given the motor solution node allocation in the axial direction from the head end to nozzle exit plane), in sequence with additional equations for structural motion and propellant burning rate as described next.

B. Equations for Structural Motion

Structural vibration can play a significant role in nonsteady SRM internal ballistic behavior, as evidenced by observed changes in combustion-instability symptoms as allied to changes in the structure surrounding the internal flow (e.g., propellant-grain configuration, wall thickness, and material properties) [11,12,15]. The level of sophistication required for modeling the motor structure (propellant, casing, static-test sleeve, and nozzle) and applicable boundary conditions (load cell on the static-test stand) can vary, depending on the particular application and motor design. Loncaric et al. [16] and Montesano et al. [17] employed a finite element approach toward the structural modeling of the given motor configuration. In the present study, a cylindrical-grain configuration allows for a simpler finite difference approach via thick-wall theory, as reported in [14]. The radial deformation dynamics of the propellant/casing/sleeve are modeled by a series of independent ring elements along the length of the motor. Axial motion along the length of the structure is modeled via beam theory and bounded by the spring/damper load cell at the motor's head end. Viscous damping is applied in the radial and axial directions. Reference structural properties are assumed for an ammonium-perchlorate/hydroxyl-terminated polybutadiene (AP/HTPB) composite propellant surrounded by an aluminum casing and steel sleeve. For greater accuracy, some properties (such as the propellant/casing/sleeve assembly's natural radial frequency) may be predetermined via a finite element numerical solution, rather than via theoretical approximations.

C. Equations for Propellant Burning Rate

With respect to transient frequency-dependent burning-rate modeling, the Zel'dovich–Novozhilov (Z-N) solid-phase energy conservation approach used in the present simulation program may be represented by the following time-dependent temperature-based relationship [18]:

$$r_b^* = r_{b,\mathrm{qs}} - \frac{1}{(T_s - T_i - \Delta H_s / C_s)} \frac{\partial}{\partial t} \int_{-\infty}^{0} \Delta T \mathrm{d}y \tag{9}$$

where $r_{b,\mathrm{qs}}$ is the quasi-steady burning rate (value for the burning rate as estimated from steady-state information for a given set of local flow conditions), T_i is the initial propellant temperature, and, in this context, $\Delta T = T(y,t) - T_i$ is the temperature distribution when moving from the burning propellant surface at $y = 0$ (and $T = T_s$) to that spatial location in the propellant at which the temperature reaches T_i. At this juncture, one may note the inclusion of a net surface-heat-release term ΔH_s in the calculations. The transient heat conduction in the solid phase can be solved by an appropriate finite difference scheme. One needs to take care in setting the solid-phase spatial increment Δy to be in accordance with the Fourier stability limit $\Delta y_{\mathrm{Fo}} = (2\alpha_s \Delta t)^{1/2}$, which is a function of the chosen time increment Δt [18]. The time increment itself must be coordinated between the flow and structural-model solution systems [17].

In Eq. (9), r_b^* is the nominal (unconstrained) instantaneous burning rate, and its value at a given propellant-grain location is solved at each time increment via numerical integration of the temperature distribution through the heat-penetration zone of the solid phase. In this respect, the present numerical model differs from past numerical models (e.g., as reported by Kooker and Nelson [19] and Nelson [20]). In those cases, the thermal gradient at the propellant surface $(\partial T/\partial y|_{y=0})$ was explicitly tied to the true instantaneous burning rate r_b by a specified function and, in turn, r_b commonly tied to a variable surface temperature T_s by an Arrhenius-type expression [19]. Following this established trend, earlier versions of numerical Z-N models did not follow through on using Eq. (9) directly, but switched to a burning-rate temperature-sensitivity correlation such as [20,21]

$$\left.\frac{\partial T}{\partial y}\right|_{y=0} = \frac{r_b}{\alpha_s}\left[T_s - \frac{1}{\sigma_p}\ell_n\left(\frac{r_b}{r_{b,\mathrm{qs}}}\right) - T_i\right] \tag{10}$$

where σ_p is the pressure-based burning-rate temperature sensitivity (which itself is a function of pressure) [21]. As reported by Nelson [20], the predicted r_b augmentation using Eq. (10) was commonly lower than expected from experimental observation for a number of transient burning applications. This was commonly true when comparing Z-N model prediction by various flame-based expressions for thermal surface gradient as a function of r_b, was of the general form [20]

$$\left.\frac{\partial T}{\partial y}\right|_{y=0} = g_1 r_b + \frac{g_2}{r_b} \tag{11}$$

The coefficients g_1 and g_2 may be ascertained as a function of a number of fixed and variable parameters, depending on the given model being employed [20].

Returning to the present integrated-temperature model, the actual instantaneous burning rate r_b may be found as a function of r_b^* through the empirical rate-limiting equation [18]:

$$\frac{\mathrm{d}r_b}{\mathrm{d}t} = K_b(r_b^* - r_b) \tag{12}$$

The rate-limiting coefficient K_b effectively damps the unconstrained burning rate r_b^* when, for a finite time increment Δt,

$$K_b < \frac{1}{\Delta t} \tag{13}$$

In the present approach, the surface thermal gradient is free to find its own value at a given instant. One can argue that the use of Eq. (12) or some comparable damping function, although empirical, parallels the approach taken by past researchers of using a stipulated surface thermal gradient [a form of Eq. (10) or Eq. (11)]; both approaches act to constrain the exchange of energy through the burning-surface interface, allow for some variability to better compare with a given set of experimental data, and prevent so-called burning-rate runaway

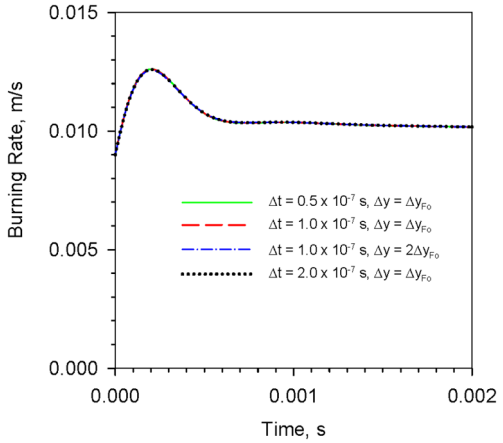

Fig. 2 Transient burning rate resulting from step input of $r_{b,\mathrm{qs}}$ from 0.009 to 0.01 m/s ($K_b = 35,000\ \mathrm{s}^{-1}$ and $\Delta H_s = 0\ \mathrm{J/kg}$).

(unstable divergence of r_b with time) [19]. As discussed in [18], the use of K_b at a set value allows for a converged solution that is independent of the increment size for Δt and Δy, as long as one respects the Fourier stability requirement noted earlier. An illustration of this point can be found in the transient burning-rate profiles of Fig. 2, in which a step input in $r_{b,\mathrm{qs}}$ from 0.9 cm/s to 1 cm/s, beginning from $t = 0$ s, produces a true instantaneous burning rate r_b that initially overshoots and then recovers and settles toward 1 cm/s in a highly damped mildly oscillatory manner. The resulting profiles are essentially the same, regardless of the various sizes for Δt and Δy that are employed.

The quasi-steady burning rate $r_{b,\mathrm{qs}}$ may be ascertained as a function of various parameters; in this study, as a function of local static pressure p, core-flow velocity u (erosive burning component), and normal/lateral/longitudinal acceleration, such that

$$r_{b,\mathrm{qs}} = r_p + r_u + r_a \tag{14}$$

The pressure-based burning component may be found through de St. Robert's law:

$$r_p = Cp^n \tag{15}$$

The flow-based erosive burning component (negative and positive) is established through the following expression [22]:

$$r_b = \left.\frac{r_b}{r_o}\right|_{\delta_r} \cdot r_o + r_e \tag{16}$$

where at lower flow speeds, the negative component resulting from a stretched combustion-zone thickness ($\delta_r > \delta_o$) may cause an appreciable drop in the base burning rate r_o, whereas at higher flow speeds, the positive erosive burning component r_e, established from a convective heat feedback premise [22], should dominate:

$$r_e = \frac{h(T_f - T_s)}{\rho_s[C_s(T_s - T_i) - \Delta H_s]} \tag{17}$$

For the preceding case, in which the base burning rate r_o is a function of the other mechanisms (pressure and acceleration), one finds the velocity-based component of burning rate from Eq. (15) via $r_u = r_b - r_o$. At higher flow speeds, r_u becomes equivalent to r_e. The effect of normal acceleration a_n resulting from radial propellant/casing/sleeve vibration may be determined via [23]

$$r_b = \left[\frac{C_p(T_f - T_s)}{C_s(T_s - T_i) - \Delta H_s}\right] \frac{(r_b + G_a/\rho_s)}{\exp[C_p\delta_o(\rho_s r_b + G_a)/k] - 1} \tag{18}$$

where the compressive effect of normal acceleration and the dissipative effect of steady or oscillatory longitudinal (or lateral if, say, for a star-grain configuration) acceleration a_ℓ is stipulated through the accelerative mass flux G_a:

$$G_a = \left\{\frac{a_n p}{r_b}\frac{\delta_o}{RT_f}\frac{r_o}{r_b}\right\}_{\phi=0\,\mathrm{deg}} \cos^2\phi_d \tag{19}$$

Note that the longitudinal/lateral-acceleration-based displacement orientation angle ϕ_d is greater than the nominal-acceleration vector orientation angle (ϕ, which is zero when only normal acceleration a_n relative to the burning propellant surface is present) [23]. One should also note that a_n is negative when acting to compress the combustion zone and is treated as zero when directed away from the zone. For the preceding case, in which the base burning rate r_o is a function of the other flow mechanisms (pressure and core flow), one finds the acceleration-based component of burning rate from Eq. (18) via $r_a = r_b - r_o$.

With respect to the burning-surface temperature T_s, one has the option of treating it as constant or allowing for its variation, depending on the phenomenological approach being taken for estimating the burning rate [18–21]. Although in the past a number of estimation models might have used a constant value for T_s, more recently, the usage of a variable T_s has become prevalent. However, based on good comparisons in general to experimental data as reported in [18], a constant T_s was employed in the present Z-N-based phenomenological numerical combustion model for the present investigation.

III. Results and Discussion

The characteristics of the reference motor for this study are listed in Table 1. The motor, based in large measure on a similar experimental motor [14], is a smaller cylindrical-grain design with an aluminum casing and static-test steel sleeve, with a relatively large length-to-diameter ratio. The motor at the time of pulsing has a moderate port-to-throat-area ratio, with a considerable propellant web thickness remaining. The predicted frequency response for the AP/HTPB propellant at three different settings for the net surface-heat-release value may be viewed in Fig. 3 (positive value for exothermic heat release). The general response is given in terms of

Table 1 Reference motor characteristics

Propellant grain length L_p	52 cm
Initial port diameter d_i	3.6 cm
Nozzle throat diameter d_t	1.6 cm
Grain/nozzle-convergence length ratio L_p/L_c	16:1
Propellant specific heat C_s	1500 J/kg · K
Propellant density ρ_s	1730 kg/m^3
Propellant thermal conductivity k_s	0.4 W/m · K
Propellant thermal diffusivity α_s	1.54×10^{-7} m^2/s
Propellant flame temperature T_f	3000 K
Propellant surface temperature T_s	1000 K
Propellant initial temperature T_i	294 K
Gas specific heat C_p	1920 J/kg · K
Specific gas constant R	320 J/kg · K
Gas thermal conductivity k	0.2 W/m · K
Gas absolute viscosity μ	8.07×10^{-5} kg/m · s
Gas specific heat ratio γ	1.2
De St. Robert exponent n	0.35
De St. Robert coefficient C	0.05 cm/s · (kPa)^n
Particle solid density ρ_m	2700 kg/m^3
Particle specific heat C_m	900 J/kg · K
Particle mass fraction α_p	0%
Propellant elastic modulus E_A	45 MPa
Propellant Poisson's ratio υ_A	0.497
Casing inner wall radius r_m	3.24 cm
Casing wall thickness h_B	0.127 cm
Casing material density ρ_B	2700 kg/m^3
Casing elastic modulus E_B	80 GPa
Casing material Poisson's ratio υ_B	0.33
Sleeve wall thickness h_C	0.47 cm
Sleeve material density ρ_C	7850 kg/m^3
Sleeve elastic modulus E_C	200 GPa
Sleeve material Poisson's ratio υ_C	0.30
Casing/propellant radial damping ratio ξ_R	0.35
Casing/propellant longitudinal damping ratio ξ_L	0.10

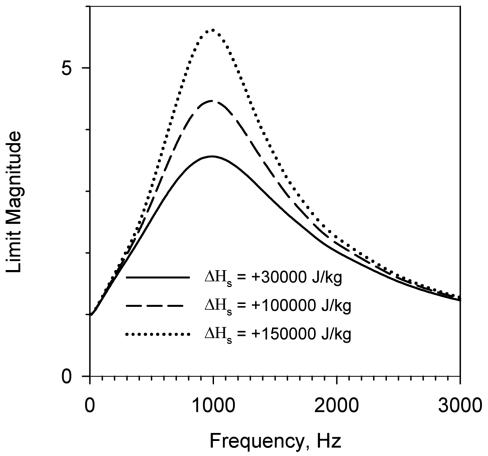

Fig. 3 Frequency response of reference propellant ($r_{b,o} = 1.27$ cm/s, $K_b = 20,000$ s^{-1}, and differing ΔH_s) in terms of nondimensional limit magnitude.

the nondimensional limit magnitude M_ℓ, defined by

$$M_\ell = \frac{r_{b,\text{peak}} - r_{b,o}}{r_{b,\text{qs,peak}} - r_{b,o}} \tag{20}$$

where the reference burning rate $r_{b,o}$ in this case is the motor's approximate mean burning rate at the point of pulsing (1.27 cm/s). The propellant's resonant frequency f_r is set via the value of K_b (20,000 s^{-1}) to be on the order of 1 kHz (a value within the range of what might be expected for this type of composite propellant at that base burning rate). This value for f_r is, in fact, relatively close to the fundamental longitudinal acoustic frequency f_{1L} of the combustion chamber, providing examples later in this paper that are close to the worst-case scenario for susceptibility to axial-combustion-instability symptoms. For the example simulation results presented in this paper, it is being assumed that the frequency-dependent combustion-response behavior of the propellant noted earlier does not change with the addition of the inert particles into the propellant. It should be acknowledged that, in practice, especially with the use of reactive particles/additives [10,11], one might anticipate that there would be some change in this regard. As noted by the example results of [18], one can potentially adjust K_b and/or ΔH_s in the present transient-combustion model to conform to such a potential change in behavior, given sufficient experimental information.

An initial pulsed-firing simulation run is completed as a starting reference for this study, in which no particles are present and no other suppression technique is applied. In Fig. 4 for head-end pressure p_c as a function of time, one can see that at some point, the principal compression wave reaches its quasi-equilibrium strength from an initial disturbance pressure Δp_d of 2 atm, with the sustained compression wave front arriving about every 1 ms, oscillating at the fundamental frequency f_{1L} of 1 kHz. The base pressure is not appreciably elevated over the nominal operating chamber pressure. The effect of normal acceleration on the burning process [related to the radial vibration of the motor propellant/casing (see [14,24])] has been nullified for this simulation (to isolate a frequency-dependent Z-N combustion response as the predominant instability-symptom driver for this set of runs), which is a factor in reducing the development of a dc shift. One can note that the pressure wave's limit magnitude (Δp_w, peak to trough) is decreasing gradually with time after first reaching its quasi-equilibrium level, as the cylindrical grain burns back and the base pressure rises.

One can refer to Fig. 5 for the pressure–time profile for the same motor, but now with 5% particle loading (by mass) of inert spherical aluminum particles with a mean 12-μm diameter. Of course, in practice, the aluminum particles would, in fact, be reactive (burning) and, as a result, continually decreasing in diameter with particle surface regression when moving aft toward the nozzle. Given the scope of the present investigation, calculations for particle regression

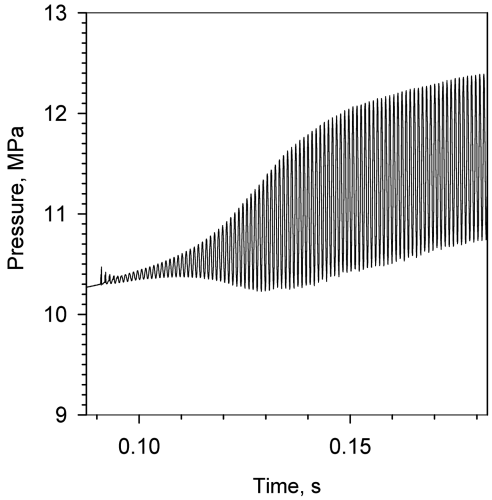

Fig. 4 Predicted head-end pressure–time profile for the reference motor ($K_b = 20,000$ s^{-1}, $\Delta H_s = 150,000$ J/kg, $\Delta p_d = 2$ atm, and $\alpha_p = 0\%$) with acceleration nullified.

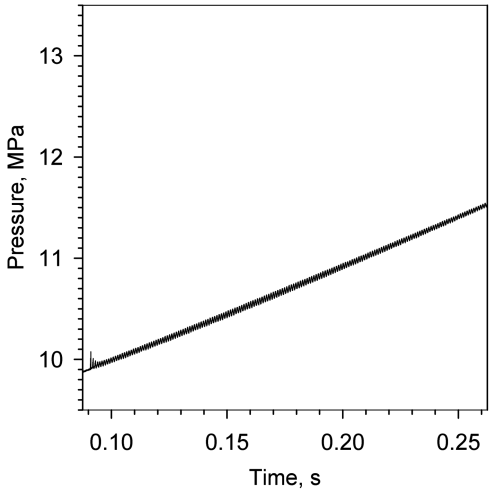

Fig. 5 Predicted head-end pressure-wave profile for the reference motor ($K_b = 20,000$ s^{-1}, $\Delta H_s = 150,000$ J/kg, and $\Delta p_d = 2$ atm) with acceleration nullified and 5% 12 μ Al particle loading by mass.

were not done; one can consider the mean inert aluminum-particle diameter as a reference size, providing results that may prove useful as a guideline when one moves to inclusion of particle burning in the computational model. Observing the results of Fig. 4, suppression of axial-wave development after an initial 2 atm pulse is nearly complete. The limit magnitude of the sustained pressure wave at 0.26 s is about 0.042 MPa (Δp_w), compared with 1.42 MPa for the 0% loading case noted earlier ($\Delta p_{w,\text{peak}}$), giving a nondimensional attenuation M_a, defined by

$$M_a = \frac{\Delta p_{w,\text{peak}} - \Delta p_w}{\Delta p_{w,\text{peak}}} \tag{21}$$

a value of 0.97, noting that a value of unity is complete suppression. Historically, suppression of high-frequency tangential and radial pressure waves in SRMs by the use of particles in the range of 1 to 3% loading by mass has been, in general, largely successful [10]. In the case of axial pressure waves, the effectiveness of particles from 1 to over 20% loading at suppressing wave development has been less consistent, relative to the previously mentioned transverse cases [11]. In the case of Fig. 4, remembering that acceleration as a factor has been nullified in the combustion process, a loading of 5% at 12 μm appears to effectively suppress axial-wave development in this particular motor, at this point in its firing.

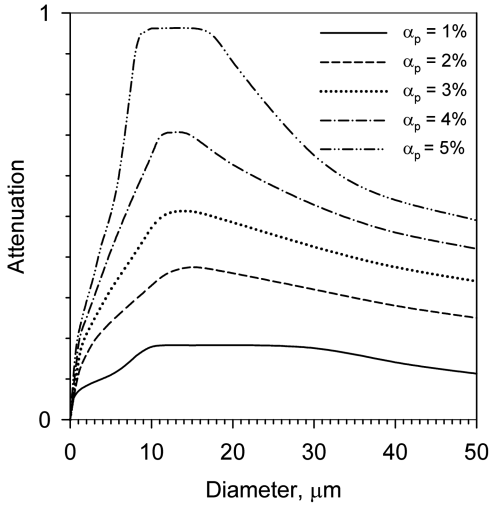

Fig. 6 Nondimensional attenuation as a function of particle diameter and loading for the reference motor with acceleration nullified.

An attenuation map for the motor is provided in Fig. 6, where various M_a curves are displayed as a function of aluminum-particle diameter, with each curve being at a particular loading percentage. The case of Fig. 5 is the approximate peak M_a point of the 5% loading curve in Fig. 6. The x axis represents, in essence, the 0% loading case (no suppression at any particle diameter). The same juncture in the firing simulations is the time reference for each point (0.26 s). Dobbins and Temkin [25], via acoustic (weak-wave) theory for low-Reynolds-number relative flow of a gas–particle mixture, reported the following well-known relation for the optimum particle diameter d_{opt} when attenuating pressure waves:

$$d_{\text{opt}} = \sqrt{\frac{9\mu}{\pi f \rho_m}} \tag{22}$$

where μ is the gas absolute viscosity, ρ_m is the particle solid density, and f is the frequency of the oscillating axial pressure wave. For the present motor, Eq. (22) would suggest a d_{opt} of around 9.2 μm, whereas Fig. 6 suggests that peak attenuation occurs at particle diameters of around 10 to 25 μm at very low loadings (around 1% for α_p, the peak appears as a plateau range), narrowing and dropping somewhat toward 12 μm as one increases the loading from 1 toward 5%, and then again a spreading range (plateau peak) from that figure of 12 μm at even higher loadings. It is not surprising that there would be a difference from the predicted acoustic-theory attenuation, given that the low-speed weak-wave assumptions inherent in Eq. (22) are not being presumed when generating the higher-flow-speed numerical results of Fig. 6, specifically when both laminar- and turbulent-flow drag between the spherical particles and gas may, in fact, be present as a predominant attenuation/loss mechanism. Note that heat transfer between particles and gas in the central flow is typically considered as a secondary effect in this attenuation process, and as pointed out earlier, particle/burning-surface interaction effects on combustion-response behavior are being neglected for these examples.

Returning to the reference motor case with no particle loading, inclusion of the solid propellant's sensitivity to normal acceleration results in a much more active motor, as evidenced in Fig. 7. The dc shift later in the firing is quite large (on the order of 5 MPa), as is the limit wave magnitude. In this regard, $\Delta p_{w,\text{peak}}$ is approximately 10.2 MPa at 0.26 s, compared with 9.5 MPa at 0.16 s, indicating a slow increase in the pressure wave's limit strength after the large dc shift is attained. The traveling axial pressure wave has a steep shock front, compared with the shallower wave front of the previous non-acceleration-sensitive case of Fig. 3 (see Fig. 8 for a wave profile comparison).

An example effect of inert particle loading on the acceleration-sensitive motor is given in Fig. 9. Here, at a loading of 2% and

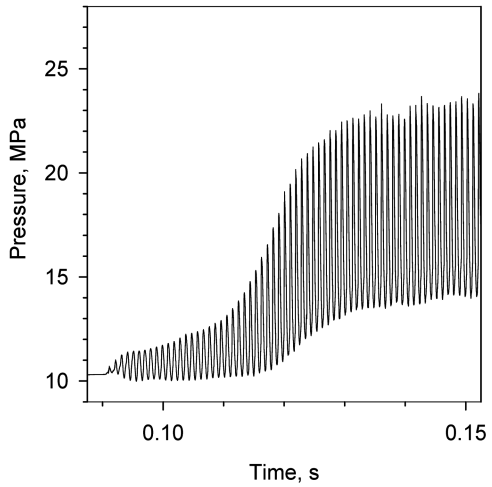

Fig. 7 Predicted head-end pressure–time profile for the reference motor ($K_b = 20,000\ \text{s}^{-1}$, $\Delta H_s = 150,000\ \text{J/kg}$, $\Delta p_d = 2\ \text{atm}$, and $\alpha_p = 0\%$) with acceleration active.

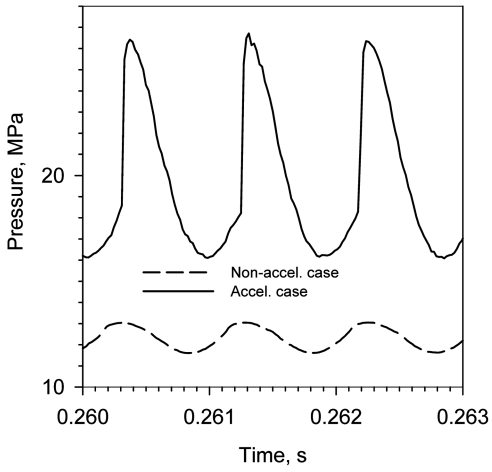

Fig. 8 Predicted head-end pressure-wave profiles for the reference motor ($K_b = 20,000\ \text{s}^{-1}$, $\Delta H_s = 150,000\ \text{J/kg}$, $\Delta p_d = 2\ \text{atm}$, and $\alpha_p = 0\%$) with acceleration inactive and active.

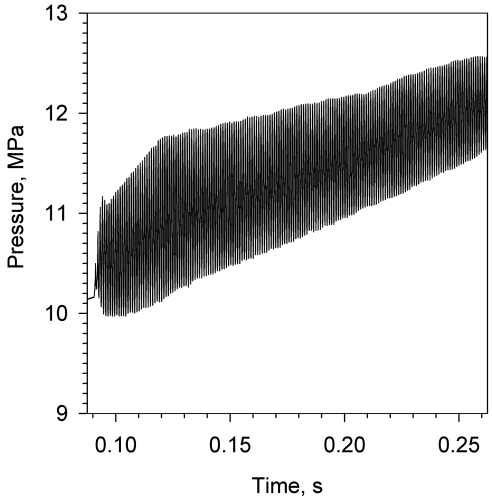

Fig. 9 Predicted head-end pressure-wave profile for the reference motor ($K_b = 20,000\ \text{s}^{-1}$, $\Delta H_s = 150,000\ \text{J/kg}$, and $\Delta p_d = 2\ \text{atm}$) with acceleration active and 2% 14 μ Al particle loading by mass.

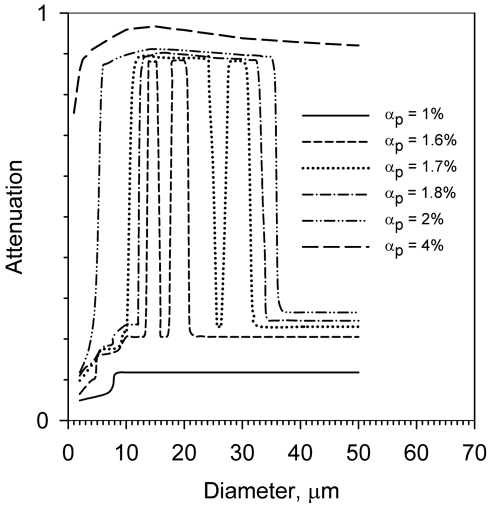

Fig. 10 Nondimensional attenuation as a function of particle diameter and loading for the reference motor with acceleration active.

particle diameter of 14 μm, after an initial 2 atm disturbance, the limit Δp_w at 0.26 s is about 0.91 MPa, or an attenuation M_a of 0.911. One can see that after reaching quasi-equilibrium early on, the pressure wave's limit magnitude tends to decrease with time. As done for the previous case, an overall particle attenuation map for the preceding acceleration-sensitive motor is provided in Fig. 10. Various M_a curves are displayed as a function of aluminum-particle diameter, with each curve being at a particular loading percentage. Moving from the 0% line (x axis of the map) to 1% particle loading, one can see the formation of an extended lower-plateau region for attenuation, from an 8 μm diameter and above at the 1% point. A higher-plateau region (in which a substantially higher attenuation exists) arises and spreads from the lower plateau (eventually absorbing the lower plateau) as particle loading moves from above 1.6% (with two transitioning peaks in the vicinity of 14 and 19 μm particle diameters initially) toward 2%. From 2 to 4% loading, one sees a further spreading and heightening of the upper plateau to smaller and larger particle diameters.

IV. Conclusions

A numerical evaluation of nonburning particles within the flow as a means for suppressing axial-pressure-wave development has been completed for a reference cylindrical-grain composite-propellant motor. When one includes the effect of normal acceleration (structural vibration) on the burning process, the attenuation behavior of the particles is altered substantially from the baseline Z-N combustion-response results. This is clearly reflected by their respective attenuation maps. If this or a comparable numerical model proves to be suitably accurate, such maps could prove to be a useful tool for motor designers evaluating their own motor configurations for instability behavior. In either case, the ability of particles to suppress axial-wave development by their presence in the core flow is evident at relatively low loading percentages; these results would appear to be consistent with experimental experience. Although supporting elements of the numerical model (such as those for propellant burning rate and structural vibration) have been shown to correlate well to quasi-steady and transient experimental data, it is acknowledged that the comparison with experimental observation of the principal results of this paper (e.g., limit-pressure-wave strength as a function of particle size and loading percentage) would, at this juncture, be better categorized as qualitative, until a direct comparison with various experimental data can be done. Although not a principal focus of the current study, the effect of particle/burning-surface interactions altering the combustion-response behavior of the propellant may, in practice, lead to even further suppression of instability symptoms than that illustrated by the example results shown in this paper.

Acknowledgments

The author wishes to acknowledge the valuable discussions with Luigi De Luca concerning the past efforts of various researchers at numerically modeling the transient burning rate in solid propellants, which allowed for important additions to this paper. Similarly, the author thanks Woodward Waesche for his communications concerning instability suppression and particle/burning-surface interaction effects, which have also allowed for important additions to the present paper.

References

[1] Brownlee, W. G., "Nonlinear Axial Combustion Instability in Solid Propellant Motors," *AIAA Journal*, Vol. 2, No. 2, Feb. 1964, pp. 275–284.
doi:10.2514/3.2303

[2] Price, E. W., "Solid Rocket Combustion Instability—An American Historical Account," *Nonsteady Burning and Combustion Stability of Solid Propellants*, edited by De Luca, L., Price, E. W., and Summerfield, M., Progress in Astronautics and Aeronautics, AIAA, Washington, D.C., Vol. 143, 1992, pp. 1–16.

[3] Barrère, M., "Introduction to Nonsteady Burning and Combustion Instability," *Nonsteady Burning and Combustion Stability of Solid Propellants*, edited by De Luca, L., Price, E. W., and Summerfield, M., Progress in Astronautics and Aeronautics, AIAA, Washington, D.C., Vol. 143, 1992, pp. 17–58.

[4] Culick, F. E. C., "Prediction of the Stability of Unsteady Motions in Solid-Propellant Rocket Motors," *Nonsteady Burning and Combustion Stability of Solid Propellants*, edited by De Luca, L., Price, E. W., and Summerfield, M., Progress in Astronautics and Aeronautics, AIAA, Washington, D.C., Vol. 143, 1992, pp. 719–780.

[5] Fishbach, S. R., Majdalani, J., and Flandro, G. A., "Acoustic Instability of the Slab Rocket Motor," *Journal of Propulsion and Power*, Vol. 23, No. 1, Jan.–Feb. 2007, pp. 146–157.
doi:10.2514/1.14794

[6] Kooker, D. E., and Zinn, B. T., "Triggering Axial Instabilities in Solid Rockets: Numerical Predictions," AIAA Paper 73-1298, Nov. 1973.

[7] Baum, J. D., and Levine, J. N., "Modeling of Nonlinear Longitudinal Instability in Solid Rocket Motors," *Acta Astronautica*, Vol. 13, Nos. 6/7, 1986, pp. 339–348.
doi:10.1016/0094-5765(86)90089-5

[8] Ramohalli, K., "Technologies and Techniques for Instability Suppression in Motors," *Nonsteady Burning and Combustion Stability of Solid Propellants*, edited by De Luca, L., Price, E. W., and Summerfield, M., Progress in Astronautics and Aeronautics, AIAA, Washington, D.C., Vol. 143, 1992, pp. 805–848.

[9] Price, E. W., "Experimental Observations of Combustion Instability," *Fundamentals of Solid-Propellant Combustion*, edited by Kuo, K. K., and Summerfield, M., Progress in Astronautics and Aeronautics, AIAA, Washington, D.C., Vol. 90, 1984, pp. 733–790.

[10] Waesche, R. H. W., "Mechanisms and Methods of Suppression of Combustion Instability by Metallic Additives," *Journal of Propulsion and Power*, Vol. 15, No. 6, Nov.–Dec. 1999, pp. 919–922.
doi:10.2514/2.5517

[11] Blomshield, F. S., "Historical Perspective of Combustion Instability in Motors: Case Studies," AIAA Paper 2001-3875, July 2001.

[12] Dotson, K. W., and Sako, B. H., "Interaction Between Solid Rocket Motor Internal Flow and Structure During Flight," *Journal of Propulsion and Power*, Vol. 23, No. 1, Jan.–Feb. 2007, pp. 140–145.
doi:10.2514/1.20477

[13] Gottlieb, J. J., and Greatrix, D. R., "Numerical Study of the Effects of Longitudinal Acceleration on Solid Rocket Motor Internal Ballistics," *Journal of Fluids Engineering*, Vol. 114, No. 3, Sept. 1992, pp. 404–410.
doi:10.1115/1.2910045

[14] Greatrix, D. R., and Harris, P. G., "Structural Vibration Considerations for Solid Rocket Internal Ballistics Modeling," AIAA Paper 2000-3804, July 2000.

[15] Krier, H., Surzhikov, S. T., and Glick, R. L., "Prediction of the Effects of Acceleration on the Burning of AP/HTPB Solid Propellants," AIAA Paper 2001-0343, Jan. 2001.

[16] Loncaric, S., Greatrix, D. R., and Fawaz, Z., "Star-Grain Rocket Motor —Nonsteady Internal Ballistics," *Aerospace Science and Technology*, Vol. 8, No. 1, Jan. 2004, pp. 47–55.
doi:10.1016/j.ast.2003.09.001

[17] Montesano, J., Greatrix, D. R., Behdinan, K., and Fawaz, Z., "Structural Oscillation Considerations for Solid Rocket Internal Ballistics

Modeling," AIAA Paper 2005-4161, July 2005.
[18] Greatrix, D. R., "Transient Burning Rate Model for Solid Rocket Motor Internal Ballistic Simulations," *International Journal of Aerospace Engineering*, Vol. 2008, 2008, Paper 826070. doi:10.1155/2008/826070
[19] Kooker, D. E., and Nelson, C. W., "Numerical Solution of Solid Propellant Transient Combustion," *Journal of Heat Transfer*, Vol. 101, May 1979, pp. 359–364.
[20] Nelson, C. W., "Response of Three Types of Transient Combustion Models to Gun Pressurization," *Combustion and Flame*, Vol. 32, No. 3, July 1978, pp. 317–319. doi:10.1016/0010-2180(78)90106-2
[21] Kuo, K. K., Kumar, S., and Zhang, B., "Transient Burning Characteristics of JA2 Propellant Using Experimentally Determined Zel'dovich Map," AIAA Paper 2003-5270, July 2003.
[22] Greatrix, D. R., "Model for Prediction of Negative and Positive Erosive Burning," *Canadian Aeronautics and Space Journal*, Vol. 53, No. 1, Mar. 2007, pp. 13–21.
[23] Greatrix, D. R., "Parametric Analysis of Combined Acceleration Effects on Solid-Propellant Combustion," *Canadian Aeronautics and Space Journal*, Vol. 40, No. 2, June 1994, pp. 68–73.
[24] Greatrix, D. R., "Predicted Nonsteady Internal Ballistics of Cylindrical-Grain Motor," AIAA Paper 2006-4427, July 9–12, 2006.
[25] Dobbins, R. A., and Temkin, S., "Measurements of Particulate Acoustic Attenuation," *AIAA Journal*, Vol. 2, No. 6, June 1964, pp. 1106–1111. doi:10.2514/3.2483

S. Son
Associate Editor